

Practical Advantage of Classical Communication in Entanglement Detection

Wen-Bo Xing,^{1,2,3,4,*} Min-Yu Lv,^{1,2,*} Lingxia Zhang,^{3,4,*} Yu Guo,^{1,2} Mirjam Weilenmann,⁵ Zhaohui Wei,^{6,7} Chuan-Feng Li,^{1,2,8} Guang-Can Guo,^{1,2,8} Xiao-Min Hu,^{1,2,8,†} Bi-Heng Liu,^{1,2,8,‡} Miguel Navascués,^{9,§} and Zizhu Wang^{3,4,¶}

¹CAS Key Laboratory of Quantum Information,
University of Science and Technology of China, Hefei 230026,
China

²CAS Center For Excellence in Quantum Information and Quantum Physics,
University of Science and Technology of China, Hefei, 230026,
China

³Institute of Fundamental and Frontier Sciences,
University of Electronic Science and Technology of China,
611731, Chengdu,
China

⁴Key Laboratory of Quantum Physics and Photonic Quantum Information,
Ministry of Education,
University of Electronic Science and Technology of China,
611731, Chengdu,
China

⁵Inria, Télécom - LTCl,
Institut Polytechnique de Paris,
91120 Palaiseau,
France

⁶Yau Mathematical Sciences Center,
Tsinghua University, Beijing 100084,
China

⁷Yanqi Lake Beijing Institute of Mathematical Sciences and Applications, Beijing 101407,
China

⁸Hefei National Laboratory,
University of Science and Technology of China, Hefei 230088,
China

⁹IQOQI-Vienna, Austrian Academy of Sciences,
Boltzmanngasse 3, 1090 Wien,
Austria

Entanglement is the cornerstone of quantum communication, yet conventional detection relies solely on local measurements. In this work, we present a unified theoretical and experimental framework demonstrating that one-way local operations and classical communication (1-LOCC) can significantly outperform purely local measurements in detecting high-dimensional quantum entanglement. By casting the entanglement detection problem as a semidefinite program (SDP), we derive protocols that minimize false negatives at fixed false-positive rates. A variational generative machine-learning algorithm efficiently searches over high-dimensional parameter spaces, identifying states and measurement strategies that exhibit a clear 1-LOCC advantage. Experimentally, we realize a genuine event-ready protocol on a three-dimensional photonic entanglement source, employing fiber delays as short-lived quantum memories. We implement rapid, FPGA-based sampling of the optimized probabilistic instructions, allowing Bob's measurement settings to adapt to Alice's outcomes in real time. Our results validate the predicted 1-LOCC advantage in a realistic noisy setting and reduce the experimental trials needed to certify entanglement. These findings mark a step toward scalable, adaptive entanglement detection methods crucial for quantum networks and computing, paving the way for more efficient generation and verification of high-dimensional entangled states.

Quantum entanglement (Gühne and Tóth, 2009; Horodecki *et al.*, 2009; Plenio and Virmani, 2007) is a necessary ingredient for most quantum communication protocols, such as dense coding (Guo *et al.*, 2019; Hu *et al.*, 2018), quantum teleportation (Bennett *et al.*, 1993; Hu *et al.*, 2023) and device-independent quantum cryptography (Acín *et al.*, 2007). The reliable distribution

* These authors contributed equally to this work

† huxm@ustc.edu.cn

‡ bhlui@ustc.edu.cn

§ miguel.navascues@oeaw.ac.at

¶ zizhu@ustc.edu.cn

and detection of entanglement between separate labs is therefore key to exploit the possibilities of a future quantum internet.

Detecting entanglement in an experimental system is a two-part process (Bavaresco *et al.*, 2018; Doherty *et al.*, 2005; Malik *et al.*, 2016; Tóth *et al.*, 2015): first, one needs to gather experimental data; second, one needs to argue, on the basis of the data, that the underlying quantum state is, in effect, entangled. Traditionally, the first part of the process has been tackled through full state tomography (Smithey *et al.*, 1993); the non-separability of the resulting state is then established through general mathematical tools, such as the Peres-Horodecki criterion (Peres, 1996) or the Doherty-Parrilo-Spedalieri (DPS) hierarchy of semidefinite programs (Doherty *et al.*, 2002).

Full state tomography of a bipartite quantum system of local dimension d requires $O(d^4)$ independent preparations of the state, as well as $O(d^4)$ different measurement settings. Therefore, as d grows, the time required for the detection of high dimensional entanglement soon becomes prohibitive. This observation motivated a different approach, based on entanglement witnesses (Terhal and Vollbrecht, 2000). Namely, in order to certify entanglement, rather than estimating the full density matrix of the state, it is enough to estimate the average of a certain bipartite Hermitian operator: the entanglement witness. This task typically requires fewer local measurements and state preparations (Flammia and Liu, 2011). It also raises the question of how to estimate the value of said witness efficiently, or, more generally, given access to such a minimal set of measurements, how to certify entanglement with confidence with a modicum of state preparations, i.e., how to construct the best witness for the task at hand.

Typically, the value of an entanglement witness W is determined through local operations (LO), i.e., entanglement detection protocols where the measurement settings for each subsystem are chosen independently. After many rounds, measurement settings and outcomes are shared and the value of W can be estimated without the need of storing any quantum state. However, it turns out that access to an (even relatively short-lived) quantum memory can make entanglement detection more efficient, without changing the local measurements to be performed. Specifically, one can implement a 1-way Local Operations and Classical Communication (1-LOCC) protocol, where the choice of measurement on one subsystem depends on the setting and the outcome of the other.

The implementation of event-ready LOCC protocols in high-dimensional systems presents significant technical challenges due to the stringent requirements for a high dimension quantum memory (Dong *et al.*, 2023) and high-speed real-time control for adaptive high-dimensional measurements (Sund *et al.*, 2023). These challenges are further exacerbated by the complexity of preparing and certifying high-dimensional quantum systems, where the number of measurement settings and classical communication

steps grows quadratically with the dimension (Wang *et al.*, 2018). So far, numerous entanglement-based LOCC operations have been successfully implemented in the qubit domain for tasks such as distributed quantum computing (Carrera Vazquez *et al.*, 2024; Liu *et al.*, 2024), entanglement extraction (Yamamoto *et al.*, 2003), entanglement swapping and distribution (Pompili *et al.*, 2021), teleportation (Chou *et al.*, 2018; Hermans *et al.*, 2022; Jin *et al.*, 2010; Krauter *et al.*, 2013; Ma *et al.*, 2012; Pfaff *et al.*, 2014; Takeda *et al.*, 2013), quantum state discrimination (Zhang *et al.*, 2023) and entanglement certification (Pallister *et al.*, 2018; Zhang *et al.*, 2020). However, the implementation of high-dimensional LOCC operations remains elusive.

Notably, (Weilenmann *et al.*, 2021) has shown theoretically that for specific quantum states, some 1-LOCC entanglement detection protocols can achieve significantly higher statistical confidence compared to the best LO protocols, especially in the case of high-dimensional entangled states. In the context of a quantum internet, where efficient and robust entanglement detection is essential, 1-LOCC protocols are particularly advantageous as they reduce the need for repeated one-photon transmissions and enable faster calibration of experimental devices, paving the way for scalable quantum communication systems.

Experimentally demonstrating such an advantage highlights the interdependence of the theoretical and experimental sides of the problem. We first turn our experimental scenario into an optimization problem (Hu *et al.*, 2021a; Weilenmann *et al.*, 2021). However, the inputs to this problem are constrained by experimental considerations such as what states can be prepared and what measurements are possible. We in turn take these experimental constraints into another optimization problem, which we solve by using a generative machine learning algorithm (Zhang *et al.*, 2024). The solution contains experimental instructions which can be directly used in state preparation and protocol execution. Probabilistic instructions for the protocols are loaded into a field programmable gate array (FPGA) chip, which controls electro-optic modulators (EOMs) to enable fast real-time control of measurements, essential ingredients for implementing classical communication. For entanglement detection in 3-dimensional states, we verify that the probability for false negatives of the single-shot protocol is smaller than that of any LO protocol with the same probability of false positives. Repeated realizations of the single-shot protocol would thus certify entanglement with a p value impossible to achieve through LO methods (Araújo *et al.*, 2020).

CONCEPTUAL SETUP

Our results are obtained in the following setup. Consider the experimental scenario where Alice and Bob aim to certify the entanglement of a shared quantum state ρ with a set of local measurements $\{A_x^a\}$ ($\{B_y^b\}$), where x (y) are labels

for measurement settings and a (b) are labels for the corresponding outcomes. The entanglement status, γ , which can be Y (yes) or N (no), is computed as a random function of the labels a, b, x, y .

This random function, together with the probabilistic choice of measurements, are called the *protocol*. It contains the probabilistic instructions for Alice and Bob and incorporates the flexibility of the experiment. What Alice and Bob are allowed to do in each round of the experiment, and in what order, can be modeled through linear constraints on the random function. Nevertheless, the goal of the experiment is the same for all protocols: minimize the probability of errors when computing the final outcome γ . Errors manifest as either type-I (false positive) or type-II (false negative), signifying that $\gamma = Y$ when ρ is separable and $\gamma = N$ when ρ is entangled, respectively.

The experimental scenario, therefore, corresponds to finding the optimal solution of the following convex optimization problem (Hu *et al.*, 2021a; Weilenmann *et al.*, 2021):

$$\begin{aligned} \min_{P(x,y,\gamma|a,b)} \quad & p_2 \\ \text{subject to} \quad & \text{tr}(M_N \rho) = p_2, \\ & p_1 \mathbb{I} - M_Y \in S^*; \quad M_Y = \mathbb{I} - M_N \\ & M_N = \sum_{a,b,x,y} P(x,y,\gamma=N|a,b) (A_x^a \otimes B_y^b) \\ & P(x,y,\gamma|a,b) \in \mathcal{P}^{\{LO, 1-LOCC\}}, \end{aligned} \quad (1)$$

where $P(x,y,\gamma|a,b)$ gives the protocol and p_1 , the probability of type-I errors, is fixed at a reasonable value to limit the likelihood of mistakenly classifying states in the separable set S^* as entangled.

Once the target state ρ and available measurements $\{A_x^a, B_y^b\}$ are specified, problem (1) is a semi definite program (SDP), the solution is the minimal false-negative probability p_2^* . In addition, it also gives the probabilistic instructions $P(x,y,\gamma=N|a,b)^*$ on how the experiment must be carried out in each round, which allows Alice and Bob to cooperatively implement the POVM M_N^* .

In our experiments, we employ two types of protocols in Fig. 1: LO and 1-LOCC protocols, where the communication goes from Alice to Bob. The simplicity of the form $P(x,y,\gamma=N|a,b)$ masks the different theoretical and experimental constraints of these two protocols. The LO protocol stipulates that in each round of the experiment, Alice and Bob choose their measurement labels x, y by sampling from a joint probability distribution $P(x,y)$, then record the outcomes a, b to compute the final outcome γ . They effectively implement the POVM element

$$\begin{aligned} M_N^{LO} &= \sum_{a,b,x,y} P(N|x,y,a,b) P(x,y) (A_x^a \otimes B_y^b) \\ &= \sum_{a,b,x,y} P_{LO}(x,y,N|a,b) (A_x^a \otimes B_y^b), \end{aligned} \quad (2)$$

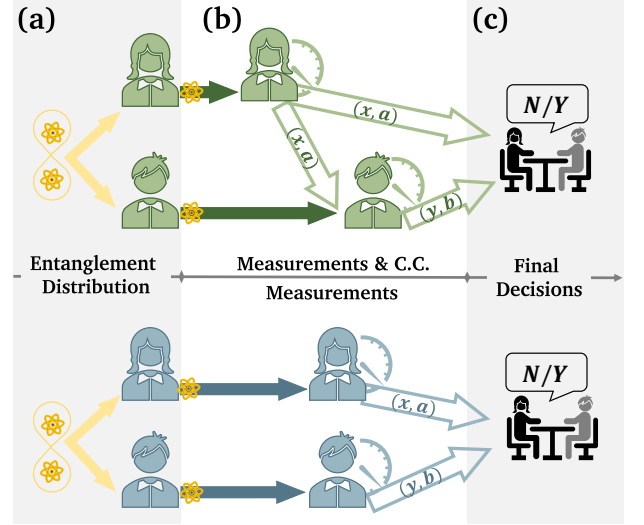


FIG. 1 Outline of the 1-LOCC (top) and LO (bottom) protocols. (a) After state preparation, the photons are distributed to Alice and Bob by quantum channels. In Phase (b) measurements are conducted and classical information is communicated after that. In 1-LOCC, Alice chooses measurement setting x randomly, obtains outcome a , and sends information (x, a) through classical channels to Bob while keeping another copy for later use. Using this information, Bob then randomly chooses measurement setting y and obtains outcome b . In LO, Alice and Bob choose x and y randomly and independently, obtaining outcomes a and b respectively. In phase (c) classical information (a, b, x, y) from Alice and Bob is collected to determine whether the state is entangled (Y) or separable (N).

with the other POVM element $M_Y^{LO} = \mathbb{I} - M_N^{LO}$.

The 1-LOCC protocol, on the other hand, is more demanding both theoretically and experimentally. At the beginning of each round, only Alice samples her measurement x from a probability distribution $P(x)$. After she obtains the outcome a , she transmits both x, a to Bob, who samples his measurement from the distribution $P(y|a, x)$. After Bob obtains his outcome b , they can compute the final outcome γ . The effective POVM is given by

$$\begin{aligned} M_N^{1-LOCC} &= \sum_{a,b,x,y} P(N|x,y,a,b) (\mathbb{I}_A \otimes B_y^b) P(y|a,x) (A_x^a \otimes \mathbb{I}_B) P(x) \\ &= \sum_{a,b,x,y} P_{1-LOCC}(x,y,N|a,b) (A_x^a \otimes B_y^b), \end{aligned} \quad (3)$$

with the other POVM element $M_Y^{1-LOCC} = \mathbb{I} - M_N^{1-LOCC}$.

The 1-LOCC protocol requires a steady supply of high-quality random numbers drawn from various complex distributions, the ability to store Bob's state while Alice carries out her operations and fast switching of Bob's measurements based on Alice's communication. Compared to the LO protocol, which only requires Alice and Bob to sample from a joint distribution $P(x,y)$, do these extra experimental costs bring an advantage in terms of having a lower probability of type-II error p_2 ?

FROM CONCEPTUAL SETUP TO EXPERIMENTAL CONSTRAINTS AND BACK

To answer the question above, we need to allow the LO and 1-LOCC versions of Eq. (1) to share as much experimental resources as possible, while comparing the two resulting p_2^* . In Eq. (1) the experimental constraints are inputs to the problem: the target state ρ to be certified and the allowed projective measurements A_x^a and B_y^b . Sharing these resources keeps the state and the allowed measurements the same for both protocols, while the probabilistic instructions $P(x, y, \gamma = N|a, b)^*$ may differ.

In an earlier work (Weilenmann *et al.*, 2021), some of us showed that there are states where there is an advantage of using 1-LOCC over LO. However, for many 2-dimensional and simple, symmetric 3-dimensional states, the type-II error probability for the two protocols is so close that implementing the classical communication does not bring any meaningful advantage. Therefore, to design our experiment, we need to find a state and a set of measurements which show a meaningful difference between the two p_2^* , under constraints imposed by modern quantum optic experiments.

Drawing on our experience with high-dimensional quantum state engineering (Hu *et al.*, 2018, 2020, 2021b), we implement a polarization-path hybrid entanglement source depicted in Fig. 2, which allows us to prepare arbitrary qutrit-qutrit states of the form

$$\rho'_{\text{exp}} = U_A \otimes I_B |\psi\rangle\langle\psi| U_A^\dagger \otimes I_B, \quad (4)$$

where $|\psi\rangle$ is provided in the Methods. The preparation of the quantum state described above requires precise angular adjustments of optical components in Fig. 2. For complex three-dimensional quantum states, determining these angular configurations is non-trivial. To achieve high-precision preparation of quantum states that demonstrate LOCC advantages, we use a systematic method that analytically maps target quantum states to angular parameters by solving a set of equations. This approach simplifies state preparation to configuring optical devices based on the computed angular parameters. Technical details are provided in the Methods. Additionally, the measurements are assumed to be projections on the computational basis, the Fourier basis, or the Gell-Mann basis, which can all be efficiently implemented using our setup.

After taking these experimental constraints into account, our initial problem Eq. (1) is transformed into a variational optimization problem with a convex optimization subproblem for the variables $\{e_1, \mathcal{X}\}$:

$$\max_{\{e_1, \mathcal{X}\}} G(\rho, p_1) = p_2^{LO*}(\rho, p_1) - p_2^{LOCC*}(\rho, p_1) \quad , \quad (5)$$

where $\mathcal{X} = \{\phi, \theta \in \mathbb{R}, \lambda_A \in \mathbb{R}^{3^2}\}$ is the parameter space of state preparation (A1) and e_1 is the parameter of false-positive error probability, which is formulated as $p_1 = (\tanh(e_1) + 1)/2$.

While $G(\rho, p_1)$ in Eq. (5) quantifies the advantage of one-way communication in entanglement detection for the state ρ with given type-I error probability p_1 , finding optimal or near-optimal solutions to Eq. (5) poses a challenge. Using naïve gradient descent algorithms requires evaluating dozens of convex optimization problems for each gradient evaluation. The algorithms also get trapped easily in local minima. To overcome these obstacles, we devised an optimization algorithm based on deep generative neural networks to solve this problem. The resulting Variational Generative Optimization Network (VGON) effectively outperforms naïve gradient descent algorithms by greatly reducing the optimization time for Eq. (5) (Zhang *et al.*, 2024).

After a near-optimal solution to Eq. (5) has been found by VGON, it gives us the target state ρ^* (The expression and the angles required for preparation are given in the Supplementary Information), the corresponding p_2^* values as $p_2^{LO*} = 0.0944$ and $p_2^{LOCC*} = 0.0283$, with $p_1 = 0.7481$, resulting in a gap of $G = 0.0661$, and two sets of instructions $P_{1-LOCC}^*(x, y, N|a, b)$, $P_{LO}^*(x, y, N|a, b)$. The explicit state, corresponding experimental parameters, and resulting instructions are detailed in the Supplementary Information. Each instruction set is made of smaller distributions: for the 1-LOCC set, we have $P^*(x)$, $P^*(y|a, x)$, $P_{1-LOCC}^*(N|x, y, a, b)$; for the LO set, we have $P^*(x, y)$ and $P_{LO}^*(N|x, y, a, b)$. In our experiment, samples from these probability distributions are stored in an FPGA chip, which serves as its nerve center.

EXPERIMENTAL SETUP AND RESULT ANALYSIS

We closely follow our entanglement detection scenario when implementing the 1-LOCC protocol. At the beginning of each experimental round, the entangled state of the target ρ^* is prepared by setting the HWPs and LCs in Fig. 2. Alice then measures $x \in \{0, 1, 2\}$ and obtains outcome a . She communicates x, a to Bob, who samples y from $P(y|a, x)$ and commands the FPGA to configure the EOMs to prepare the measurement y . Meanwhile, his photon is temporarily stored in a simple quantum memory until his measurement is ready. The EOMs have a repetition rate of 10 MHz and the quantum memory takes the form of a photon delay mechanism, implemented using two 50 m fibers. After Bob obtains his outcome b , the Time-to-Digital Converter (TDC) records and analyzes the coincidence count (a, b) . The final outcome (coincidence count) is randomly rejected with probability $P_{1-LOCC}^*(N|a, b, x, y)$, completing one round of the 1-LOCC process. Repeating for a few million rounds allows us to collect statistics of coincidence counts to estimate the false negative error probability $p_2^{1-LOCC*}$ for the 1-LOCC protocol. Experimental details can be found in Supplementary Information.

The stability of the entanglement source and our experimental goal stipulates that the best way to control for the effect of classical communication is to keep as much of the

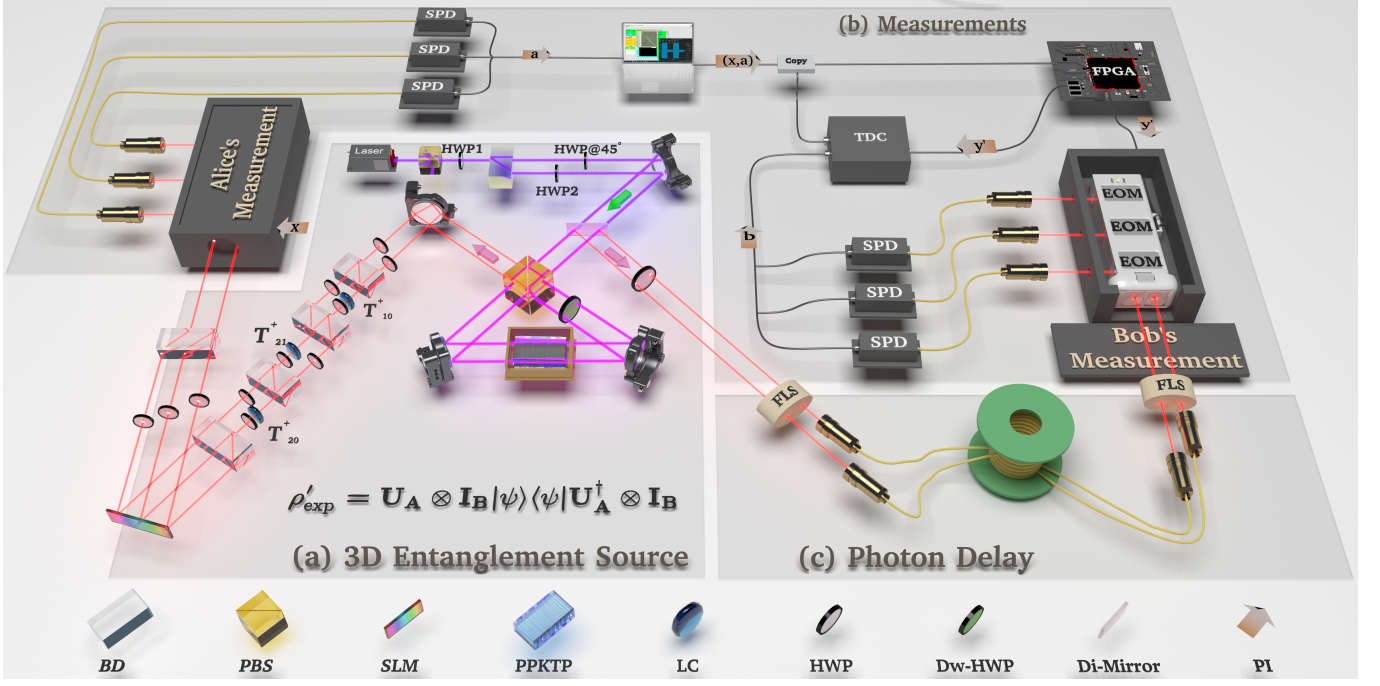


FIG. 2 Experimental setup. **(a) 3D Entanglement Source:** 3D entangled photons are generated via spontaneous parametric down-conversion (SPDC) in a PPKTP crystal, pumped by a 404 nm continuous-wave laser with 20 mW power, using polarization-path hybrid encoding (Hu *et al.*, 2018, 2021a, 2020). By adjusting HWP1-2, $|\psi\rangle$ in Eq. (4) is prepared, which then undergoes Alice's unitary operation U_A to produce the experimental target state ρ'_{exp} . The U_A is further decomposed into three two-level unitary transformations T_{ij}^\dagger , with details provided in the Supplementary Information. **(B) Measurements:** This part is responsible for entangled photons detection and the implementation of the LOCC protocol. Both Alice's and Bob's measurement setups allow switching among three measurement bases. Bob's measurement basis y' is switched via three FPGA-controlled EOMs, where y' is influenced by Alice's measurement basis x and results a . In contrast, x is switched by the experimenter, with x determined through random number sampling. The computer and FPGA handle classical communication (acceptance/rejection), store random number tables, and control the EOM. The TDC is responsible for data acquisition and analytical decision-making (Y or N). **(c) Photon Delay:** Two 50 m fibers are used for photon delay to ensure that Bob's measurement is prepared before the arrival of the photon. BD: beam-displacer; PBS: Polarizing Beam Splitter; SLM: Spatial Light Modulator; PPKTP: Periodically Poled KTP; LC: Liquid Crystal; HWP: Half Wave Plate; Dw-HWP: Dual-wavelength Half Wave Plate; Di-Mirror: Dichroic Mirrors; PI: Probabilistic Instructions. FLS: Fiber Locking System; FPGA: Field Programmable Gate Array Chip; SPD: Single Photon Detector; TDC: Time-to-Digital Converter. Details of the experimental setup, Measurements, and FLS are provided in the Supplementary Information.

setup as possible and shuffle the rounds of LO and 1-LOCC, so that unstable experimental environments and devices will affect the two protocols equally. Therefore, instead of sampling x, y from $P^*(x, y)$, we replace $P(y|a, x)$ with $P(y|x)$, from which we get $P(x, y) = P(y|x)P(x)$. The distributions $P(x)$ for both protocols are combined into a single distribution $P_m(x)$. In each experimental round, the settings x are sampled from $P_m(x)$ and used in both protocols. To allow TDC to track which protocol is implemented in each round, $P(y|x)$ and $P(y|a, x)$ are merged by encoding the settings y of LO as $y' \in \{0, 1, 2\}$ and those from 1-LOCC as $y' \in \{3, 4, 5\}$. For each x , the FPGA switches Bob's measurement by sampling from the merged distribution $P_m(y'|a, x)$, given a and x as inputs. For $y' \in \{0, 1, 2\}$, i.e. the LO protocol is implemented, $P_m(y'|a, x)$ is the same for all a , ensuring Alice's measurement outcome does not influence Bob's choice of measurement settings. A single experimental round is complete after the TDC records a coincidence event (a, b, x, y') . The distributions mentioned

above are given in Supplementary Information.

The source in Fig. 2 generates 1200 pairs of entangled photons per second, with a coincidence efficiency of 10 % in an 8 ns coincidence window. Total data collection time is 28 minutes, resulting in about 1 million experimental rounds per protocol. After data collection and analysis, the experimental false-negative error probabilities of 1-LOCC and LO are 0.0779 and 0.1390, resulting the gap in Eq. (5) of 0.0611, indicating the advantage of classical communication in reducing statistical errors. However, to confirm the advantage of classical communication over all LO protocols for the states generated by our setup, the experimental p_2^{1-LOCC} value should be smaller than p_2^{LO} even under the most optimistic estimation. This, in turn, requires us to estimate the states ρ_{est}^{LO} and ρ_{est}^{1-LOCC} from raw experimental data. The measurement bases used in our protocols are far from tomographically complete, therefore we use an SDP to find the states which deviate the least from raw experimental data under the l^2 norm. With ρ_{est}^{LO} and ρ_{est}^{1-LOCC} , we

obtain optimistic estimations of p_2^{LO} using a set of random product states and fixed values for p_1 . Fig. 3 shows that even under these optimistic estimations, the experimental p_2 value for LOCC (blue square) still outperforms that of LO (green curve). The Methods section contains additional details on how ρ_{est}^{LO} , ρ_{est}^{1-LOCC} and the green curve are obtained.

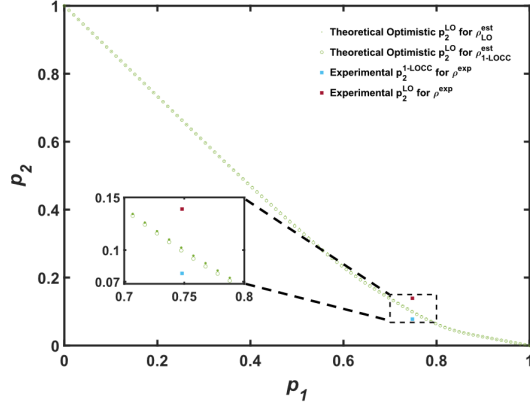


FIG. 3 Comparison of optimistic false-negative probabilities in LO with experimental and theoretical values under 1-LOCC. Green dots and circles represent optimistic p_2 values for the estimated states ρ_{LO}^{est} and ρ_{1-LOCC}^{est} under LO scenario. The experimental p_2 value (blue square) in 1-LOCC scenario is below the optimistic estimate LO curves. The red square represents the experimental p_2 value in LO scenario.

This work experimentally demonstrates the advantage of extra classical information in reducing the statistical error in entanglement certification protocols. By integrating protocols with and without classical communication in the same experimental setup, the advantage of classical information was fairly identified and quantified using short-lived memory techniques and high-speed measurement switching devices.

The experimental results align with theoretical predictions, validating the robustness of the 1-LOCC advantage even in the presence of noise. This proof-of-principle experiment highlights the potential of 1-LOCC protocols as scalable and efficient tools for detecting quantum entanglement, offering significant advancements for quantum networks and the quantum internet. Future work should focus on extending these techniques to multipartite and higher-dimensional systems, refining noise models, and exploring adaptive measurement strategies to enhance their practical applications in quantum technologies further.

ACKNOWLEDGMENTS

This work was supported by the NSFC (No. 12374338, No. 11904357, No. 12174367, No. 12204458, No. 62250073, No. 62272259), the Sichuan Provincial Key R&D Program (2024YFHZ0371), the National Key

R&D Program of China (2021YFE0113100), the Innovation Program for Quantum Science and Technology (No. 2021ZD0301200), Anhui Provincial Natural Science Foundation (No. 2408085JX002), Anhui Province Science and Technology Innovation Project (No. 202423r06050004), China Postdoctoral Science Foundation (2021M700138).

REFERENCES

- Acín, Antonio, Nicolas Brunner, Nicolas Gisin, Serge Massar, Stefano Pironio, and Valerio Scarani (2007), “Device-independent security of quantum cryptography against collective attacks,” *Phys. Rev. Lett.* **98**, 230501.
- Araújo, Mateus, Flavien Hirsch, and Marco Túlio Quintino (2020), “Bell nonlocality with a single shot,” *Quantum* **4**, 353.
- Bavaresco, Jessica, Natalia Herrera Valencia, Claude Klöckl, Matej Pivoluska, Paul Erker, Nicolai Friis, Mehul Malik, and Marcus Huber (2018), “Measurements in two bases are sufficient for certifying high-dimensional entanglement,” *Nature Physics* **14** (10), 1032–1037.
- Bennett, Charles H, Gilles Brassard, Claude Crépeau, Richard Jozsa, Asher Peres, and William K. Wootters (1993), “Teleporting an unknown quantum state via dual classical and einstein-podolsky-rosen channels,” *Phys. Rev. Lett.* **70**, 1895–1899.
- Carrera Vazquez, Almudena, Caroline Tornow, Diego Ristè, Stefan Woerner, Maika Takita, and Daniel J. Egger (2024), “Combining quantum processors with real-time classical communication,” *Nature* **636** (8041), 75–79.
- Chou, Kevin S, Jacob Z. Blumoff, Christopher S. Wang, Philip C. Reinhold, Christopher J. Axline, Yvonne Y. Gao, L. Frunzio, M. H. Devoret, Liang Jiang, and R. J. Schoelkopf (2018), “Deterministic teleportation of a quantum gate between two logical qubits,” *Nature* **561** (7723), 368–373.
- Doherty, A C, Pablo A. Parrilo, and Federico M. Spedalieri (2002), “Distinguishing separable and entangled states,” *Phys. Rev. Lett.* **88**, 187904.
- Doherty, Andrew C, Pablo A. Parrilo, and Federico M. Spedalieri (2005), “Detecting multipartite entanglement,” *Phys. Rev. A* **71**, 032333.
- Dong, Ming-Xin, Wei-Hang Zhang, Lei Zeng, Ying-Hao Ye, Da-Chuang Li, Guang-Can Guo, Dong-Sheng Ding, and Bao-Sen Shi (2023), “Highly efficient storage of 25-dimensional photonic qudit in a cold-atom-based quantum memory,” *Physical Review Letters* **131** (24), 240801.
- Flammia, Steven T, and Yi-Kai Liu (2011), “Direct fidelity estimation from few pauli measurements,” *Phys. Rev. Lett.* **106**, 230501.
- Guo, Yu, Bi-Heng Liu, Chuan-Feng Li, and Guang-Can Guo (2019), “Advances in quantum dense coding,” *Advanced Quantum Technologies* **2** (5-6), 1900011.
- Gurobi Optimization, LLC, (2024), “*Gurobi Optimizer Reference Manual*,” .
- Gühne, Otfried, and Géza Tóth (2009), “Entanglement detection,” *Physics Reports* **474** (1), 1–75.
- Hermans, S L N, M. Pompili, H. K. C. Beukers, S. Baier, J. Borgegaard, and R. Hanson (2022), “Qubit teleportation between non-neighbouring nodes in a quantum network,” *Nature* **605** (7911), 663–668.
- Horodecki, Ryszard, Paweł Horodecki, Michał Horodecki, and Karol Horodecki (2009), “Quantum entanglement,” *Rev. Mod. Phys.* **81**, 865–942.

- Hu, Xiao-Min, Yu Guo, Bi-Heng Liu, Yun-Feng Huang, Chuan-Feng Li, and Guang-Can Guo (2018), “Beating the channel capacity limit for superdense coding with entangled ququarts,” *Science Advances* **4** (7), eaat9304.
- Hu, Xiao-Min, Yu Guo, Bi-Heng Liu, Chuan-Feng Li, and Guang-Can Guo (2023), “Progress in quantum teleportation,” *Nature Reviews Physics* **5** (6), 339–353.
- Hu, Xiao-Min, Wen-Bo Xing, Yu Guo, Mirjam Weilenmann, Edgar A. Aguilar, Xiaoqin Gao, Bi-Heng Liu, Yun-Feng Huang, Chuan-Feng Li, Guang-Can Guo, Zizhu Wang, and Miguel Navascués (2021a), “Optimized detection of high-dimensional entanglement,” *Phys. Rev. Lett.* **127**, 220501.
- Hu, Xiao-Min, Wen-Bo Xing, Bi-Heng Liu, De-Yong He, Huan Cao, Yu Guo, Chao Zhang, Hao Zhang, Yun-Feng Huang, Chuan-Feng Li, and Guang-Can Guo (2020), “Efficient distribution of high-dimensional entanglement through 11 km fiber,” *Optica* **7** (7), 738–743.
- Hu, Xiao-Min, Chao Zhang, Yu Guo, Fang-Xiang Wang, Wen-Bo Xing, Cen-Xiao Huang, Bi-Heng Liu, Yun-Feng Huang, Chuan-Feng Li, Guang-Can Guo, Xiaoqin Gao, Matej Pivoluska, and Marcus Huber (2021b), “Pathways for entanglement-based quantum communication in the face of high noise,” *Phys. Rev. Lett.* **127** (11), 110505.
- Jin, Xian-Min, Ji-Gang Ren, Bin Yang, Zhen-Huan Yi, Fei Zhou, Xiao-Fan Xu, Shao-Kai Wang, Dong Yang, Yuan-Feng Hu, Shuo Jiang, Tao Yang, Hao Yin, Kai Chen, Cheng-Zhi Peng, and Jian-Wei Pan (2010), “Experimental free-space quantum teleportation,” *Nature Photonics* **4** (6), 376–381.
- Krauter, H, D. Salart, C. A. Muschik, J. M. Petersen, Heng Shen, T. Fernholz, and E. S. Polzik (2013), “Deterministic quantum teleportation between distant atomic objects,” *Nature Physics* **9** (7), 400–404.
- Liu, Xiao, Xiao-Min Hu, Tian-Xiang Zhu, Chao Zhang, Yi-Xin Xiao, Jia-Le Miao, Zhong-Wen Ou, Pei-Yun Li, Bi-Heng Liu, Zong-Quan Zhou, *et al.* (2024), “Nonlocal photonic quantum gates over 7.0 km,” *Nature Communications* **15** (1), 8529.
- Ma, Xiao-Song, Thomas Herbst, Thomas Scheidl, Daqing Wang, Sebastian Kropatschek, William Naylor, Bernhard Wittmann, Alexandra Mech, Johannes Kofler, Elena Anisimova, Vadim Makarov, Thomas Jennewein, Rupert Ursin, and Anton Zeilinger (2012), “Quantum teleportation over 143 kilometres using active feed-forward,” *Nature* **489** (7415), 269–273.
- Malik, Mehul, Manuel Erhard, Marcus Huber, Mario Krenn, Robert Fickler, and Anton Zeilinger (2016), “Multi-photon entanglement in high dimensions,” *Nature Photonics* **10** (4), 248–252.
- MOSEK ApS, (2025), *The MOSEK optimization toolbox for MATLAB manual. Version 11.0.8*.
- Pallister, Sam, Noah Linden, and Ashley Montanaro (2018), “Optimal verification of entangled states with local measurements,” *Phys. Rev. Lett.* **120**, 170502.
- Peres, Asher (1996), “Separability criterion for density matrices,” *Phys. Rev. Lett.* **77**, 1413–1415.
- Pfaff, W, B. J. Hensen, H. Bernien, S. B. Van Dam, M. S. Blok, T. H. Taminiau, M. J. Tiggelman, R. N. Schouten, M. Markham, D. J. Twitchen, and R. Hanson (2014), “Unconditional quantum teleportation between distant solid-state quantum bits,” *Science* **345** (6196), 532–535.
- Plenio, Martin B, and Shashank Virmani (2007), “An introduction to entanglement measures,” *Quantum Inf. Comput.* **7** (1), 1–51.
- Pompili, M, S. L. N. Hermans, S. Baier, H. K. C. Beukers, P. C. Humphreys, R. N. Schouten, R. F. L. Vermeulen, M. J. Tiggelman, L. Dos Santos Martins, B. Dirkse, S. Wehner, and R. Hanson (2021), “Realization of a multinode quantum network of remote solid-state qubits,” *Science* **372** (6539), 259–264.
- Reck, Michael, Anton Zeilinger, Herbert J. Bernstein, and Philip Bertani (1994), “Experimental realization of any discrete unitary operator,” *Phys. Rev. Lett.* **73**, 58–61.
- Smithey, D T, M. Beck, M. G. Raymer, and A. Faridani (1993), “Measurement of the wigner distribution and the density matrix of a light mode using optical homodyne tomography: Application to squeezed states and the vacuum,” *Phys. Rev. Lett.* **70**, 1244–1247.
- Sund, Patrik I, Emma Lomonte, Stefano Paesani, Ying Wang, Jacques Carolan, Nikolai Bart, Andreas D Wieck, Arne Ludwig, Leonardo Midolo, Wolfram HP Pernice, *et al.* (2023), “High-speed thin-film lithium niobate quantum processor driven by a solid-state quantum emitter,” *Science Advances* **9** (19), eadg7268.
- Takeda, Shuntaro, Takahiro Mizuta, Maria Fuwa, Peter Van Loock, and Akira Furusawa (2013), “Deterministic quantum teleportation of photonic quantum bits by a hybrid technique,” *Nature* **500** (7462), 315–318.
- Terhal, Barbara M, and Karl Gerd H. Vollbrecht (2000), “Entanglement of formation for isotropic states,” *Phys. Rev. Lett.* **85**, 2625–2628.
- Tóth, Géza, Tobias Moroder, and Otfried Gühne (2015), “Evaluating convex roof entanglement measures,” *Phys. Rev. Lett.* **114**, 160501.
- Wang, Jianwei, Stefano Paesani, Yunhong Ding, Raffaele Santagati, Paul Skrzypczyk, Alexia Salavrakos, Jordi Tura, Remigiusz Augusiak, Laura Mančinska, Davide Bacco, *et al.* (2018), “Multidimensional quantum entanglement with large-scale integrated optics,” *Science* **360** (6386), 285–291.
- Weilenmann, Mirjam, Edgar Aguilar, and Miguel Navascués (2021), “Analysis and optimization of quantum adaptive measurement protocols with the framework of preparation games,” *Nature Communications* **12**, 4553.
- Yamamoto, Takashi, Masato Koashi, Şahin Kaya Özdemir, and Nobuyuki Imoto (2003), “Experimental extraction of an entangled photon pair from two identically decohered pairs,” *Nature* **421** (6921), 343–346.
- Zhang, Lingxia, Xiaodie Lin, Peidong Wang, Kaiyan Yang, Xiao Zeng, Zhaohui Wei, and Zizhu Wang (2024), “Variational optimization for quantum problems using deep generative networks,” *arXiv:arXiv:2404.18041 [quant-ph]*.
- Zhang, Wen-Hao, Chao Zhang, Zhe Chen, Xing-Xiang Peng, Xiao-Ye Xu, Peng Yin, Shang Yu, Xiang-Jun Ye, Yong-Jian Han, Jin-Shi Xu, Geng Chen, Chuan-Feng Li, and Guang-Can Guo (2020), “Experimental optimal verification of entangled states using local measurements,” *Phys. Rev. Lett.* **125**, 030506.
- Zhang, Xiaoqian, Maolin Luo, Guifang Yu, and Xiaoqi Zhou (2023), “Experimental discrimination of two-qubit orthogonal states via local operations and classical communication,” *Phys. Rev. A* **108**, 032215.

Appendix A: Additional Experimental Details

The quantum state $|\psi\rangle$ in Eq. 4 has the following form:

$$|\psi\rangle = \sin \frac{\theta}{2} \cos \frac{\phi}{4} |00\rangle + \sin \frac{\theta}{2} \sin \frac{\phi}{4} |11\rangle + \cos \frac{\theta}{2} |22\rangle, \quad (\text{A1})$$

where $\phi \in [0, 2\pi)$ and $\theta \in [0, \pi]$. This state is derived from the simultaneous solution of the pump beam state and the Jones calculus for HWP1 and HWP2 in Fig. 2, and is generated via SPDC.

The local unitary on Alice's side U_A is parametrized by a set of 3^2 linearly-independent skew-Hermitian matrices $\{T_j\}$ (Reck *et al.*, 1994):

$$U_A = \exp\left(\sum_{j=1}^{3^2} \lambda_j T_j\right), \quad (\text{A2})$$

where λ_j 's are 3^2 parameters, denoted as λ_A . The $\{T_j\}$ and λ_A can be expressed in terms of the operational matrices of HWP, LC, and SLM in U_A , followed by an analytical solution.

By jointly solving Eqs. (A1)-(A2), we establish a mapping between the quantum state in Eq. 4 and the angular configurations of optical components. The angles required for this experiment are provided in the Supplementary Information.

Event-ready measurements for the two protocols require sampling random numbers from three distributions: $p_m(x)$, $p_m(y|a, x)$, and $p^*(N|a, x, b, y)$, after the slight tweaking of one of the protocols. In our experiments, all random numbers were pre-generated using Mathematica. A total of 172 random number tables were generated: one for $x \in \{0, 1, 2\}$ (RTx), nine for $y' \in \{0, 1, 2, 3, 4, 5\}$ (RTy'), and 162 for $N \in \{0, 1\}$ (RTN). The explicit distributions can be found in the Supplementary Information. Before measurement, the runtime for each x setting is determined by the digit counts in RTx (e.g., if RTx contains 10 zeros, $x = 0$ is measured for 10 seconds). RTy's are stored in the FPGA, while RTNs are stored in the TDC.

The measurement begins with the experimenter configuring the setups and announcing the choice of x , i.e. x is known for all devices. Alice's result a for each detected entangled photon is transmitted to the FPGA and copied to the TDC (e.g., Fig. 2). Using each (x, a) , the FPGA selects y' from RTy' and configures Bob's measurement basis by EOMs as $y = y' \bmod 3$. Bob's result ($b \in \{0, 1, 2\}$) corresponds to B1-B3, and sends b to the TDC. The measurement configuration settings are detailed in the Supplementary Information.

At this stage, the TDC knows (a, b, x) but lacks y , preventing it from selecting RTN to sample N . To resolve this, five additional FPGA outputs are connected to the TDC: three for y and two indicating whether the measurement corresponds to the 1-LOCC or LO protocol. Using

(LO/1-LOCC, a, b, x, y), the TDC selects a random number from RTN to decide whether to reject the measurement. The experimenter counts four-body coincidence counts $[\text{LO/1-LOCC}, a, b, y]$ using the TDC. The x informs the TDC of the measurement timing but is not involved in coincidence counts. The experiment is complete after setting x three times and obtaining all measurements.

This process ensures accurate, simultaneous measurement of both protocols under identical noise conditions.

Appendix B: Estimating the experimental states and optimistic p_2 for LO

After data collection and analysis, we notice that the experimental false-negative values increased, while the gap between them remained quite large, likely due to state deviations arising from experimental imperfections. These deviations make it unreasonable to assume that theoretical expectation values perfectly align with the raw experimental data. Therefore, we estimate ρ_{exp} by finding the best state ρ_{est} which minimizes deviations from raw data quantified by the sum of squared error between nonzero raw expectation values E^{exp} and corresponding theoretical estimations. Here $E^{exp} = \{E_{(a,b,x,y)}^{exp}\}_{(a,b,x,y) \in I'}$, and $I' = \{(a, b, x, y) | P(x, y, N|a, b)^* \neq 0\}$. The resulting optimization problem is given by

$$\begin{aligned} \min_{\rho_{est}} \quad & \|E_{(a,b,x,y)}^{exp} - E_{(a,b,x,y)}\|^2 \quad (a, b, x, y) \in I' \\ \text{s.t.} \quad & E_{(a,b,x,y)} = \text{tr}(\rho_{est}(A_x^a \otimes B_y^b)) \quad (a, b, x, y) \in I' \\ & \text{tr}(\rho_{est}) = 1; \quad \rho_{est} \geq 0 \end{aligned} \quad (\text{B1})$$

where $\{E_{(a,b,x,y)}\}_{(a,b,x,y) \in I'}$ represents the theoretical expectation values for the estimated state ρ_{est} , corresponding to the raw data of local measurement pairs in the E^{exp} . The values of the objective functions obtained by cvx using the solver Mosek (MOSEK ApS, 2025), quantifying the minimum amount of correction needed to make the raw experimental data consistent with physical density matrices, are both on the order of 10^{-4} for E_{LO}^{exp} and E_{1-LOCC}^{exp} .

Taking the value of p_2 as a metric, the estimated states ρ_{est}^{LO} and ρ_{est}^{1-LOCC} more accurately represent ρ_{exp} than ρ^* , while the gaps are also consistent with the experiment (see Supplementary Information). To confirm the advantage of classical communication, we obtain an optimistic estimation of p_2 for LO protocols based on the estimated states.

Our conceptual setup, Eq. (1), corresponds to an outer approximation of the set of separable states via the dual of the first level of the DPS hierarchy. It can be seen as a pessimistic estimation of p_2 . On the other hand, an optimistic estimation can be obtained by solving the following linear programming problem, which we solve using

Gurobi (Gurobi Optimization, LLC, 2024):

$$\begin{aligned}
& \min_{P(x,y,\gamma|a,b)} p_2^{LO} \\
& \text{subject to} \quad \text{tr}(M_N \rho_{est}) = p_2, \\
& \quad \text{tr}(M_Y \rho_i) \leq p_1, i = 1, \dots, d, \\
& \quad M_N = \sum_{a,b,x,y} P(x,y,\gamma=N|a,b) (A_x^a \otimes B_y^b) \\
& \quad M_Y = \mathbb{I} - M_N \\
& \quad \sum_{\gamma} P(x,y,\gamma|a,b) = P(x,y), \quad \sum_{x,y} P(x,y) = 1.
\end{aligned} \tag{B2}$$

$\{\rho_i\}_{i=1}^d$, $d = 100,000$ are random product states that approximate the separable set from the inside. We plot the optimum solutions to Eq. (B2) against 100 different values of $0 \leq p_1 \leq 1$, which gives the green curve in Fig. (3)

Appendix C: Optimized state, protocols, and probabilistic instructions

Our research aims to experimentally demonstrate the advantages of LOCC in entanglement detection. A more efficient solution to Eq. (5) will help identify quantum states that offer greater advantages—those that are easier to measure and can be experimentally prepared. To achieve this, we have designed a variational generative optimization network (VGON) (Zhang *et al.*, 2024). The resulting state $\rho^* = |\phi^*\rangle\langle\phi^*|$, generated by the VGON, is presented below. Although it is neither regular nor symmetric, a strategy for its experimental preparation can be developed by solving a system of equations. The experiment strategy are shown in Table II.

$$|\phi^*\rangle = \begin{pmatrix} -0.2707 - 0.2859i, \\ 0.2435 + 0.2818i, \\ -0.1624 + 0.1675i, \\ 0.0932 + 0.1845i, \\ -0.1873 - 0.1474i, \\ -0.2944 + 0.2817i, \\ 0.3284 - 0.2914i, \\ 0.3043 - 0.3131i, \\ -0.0182 + 0.0503i \end{pmatrix} \tag{C1}$$

The experimental preparation strategy for ρ^* is shown in Table II for various waveplate angles. The corresponding waveplates in the table are linked to those depicted in Fig. 2.

The ρ^* 's minimal false-negative error probabilities p_2^{LO*} , $p_2^{1-LOCC*}$ and advantage G are presented in Table I. Additionally, the optimal instructions for the LO and 1-LOCC scenarios are detailed in Table VIII. The distributions associated with the construction of measurement protocols of LO and 1-LOCC M_N^{*LO} and $M_N^{*1-LOCC}$ are in Table III and Table IX. These probabilities all come from solving Eqs. (1)-(3).

Appendix D: Experimental Measurement Settings

During the measurement stage, for simplicity, the sets of local measurements available to Alice and Bob are kept the identical and fixed, in the configuration of the experimental routine computational basis shown in Eq. (D1), the Fourier basis, and the Gell-Mann basis, which are also used as known information to solve for $M_{LO_N}^*$ and $M_{1-LOCC_N}^*$.

Alice's measurements are implemented using HWP3-HWP5, as shown in Figure 4(a), with the corresponding angles specified in Table VI. The dynamic nature of the 1-LOCC requires Bob to first await information from Alice and then rapidly change basis in response to her signals, which necessitates the short-lived memory and real-time response on Bob's side. The real-time switching among the three measurement bases is initiated by Alice's signals and facilitated by various configurations of extra electro-optical modulators (EOMs) controlled by an FPGA. The experimental setup is depicted in Fig. 4(b), with the configurations of EOMs details provided in Table VII. The memory duration is determined by the response times of the EOMs and FPGA, which are 120 ns and 50 ns, respectively. To achieve the necessary delay, we employed two 50-meter optical fibers, providing a maximum delay time of approximately 245 ns, ensuring that Bob's measurement basis was adequately prepared before the arrival of the photon to be measured.

$$\begin{aligned}
A_1 &= \{|0\rangle, |1\rangle, |2\rangle\}, \\
A_2 &= \left\{ \frac{1}{\sqrt{3}}(|0\rangle + e^{-i\frac{2\pi}{3}}|1\rangle + e^{-i\frac{2\pi}{3}}|2\rangle), \right. \\
& \quad \left. \frac{1}{\sqrt{3}}(|0\rangle + e^{-i\frac{2\pi}{3}}|1\rangle + e^{-i\frac{2\pi}{3}}|2\rangle), \right. \\
& \quad \left. \frac{1}{\sqrt{3}}(|0\rangle + |1\rangle + |2\rangle) \right\}, \\
A_3 &= \left\{ \frac{1}{\sqrt{2}}(|1\rangle - |2\rangle), |0\rangle, \frac{1}{\sqrt{2}}(|1\rangle + |2\rangle) \right\}.
\end{aligned} \tag{D1}$$

Appendix E: The Photon Delay Mechanism

During 1-LOCC, it is critical that Bob's photon arrives after the FPGA's electrical output to ensure that his measurement basis is ready. In our actual experiment, the response time of FPGA and EOM is approximately 170 ns, so we introduce a 50 m fiber delay, which provides a waiting time of 250 ns for the optical signal. But this will bring about a problem, i.e., the phase between two paths is not stable without active feedback. So we use an 830nm light as reference light to lock the phase of entanglement photon which is 808nm in the fiber locking system (Hu *et al.*, 2020).

As shown in Fig 5, two narrowband filters are used to separate entangled photons and reference light. The reference light is emitted by a semiconductor laser and then passes through a beam displacer, divided into two beams. To reduce disturbance to entanglement photons, the refer-

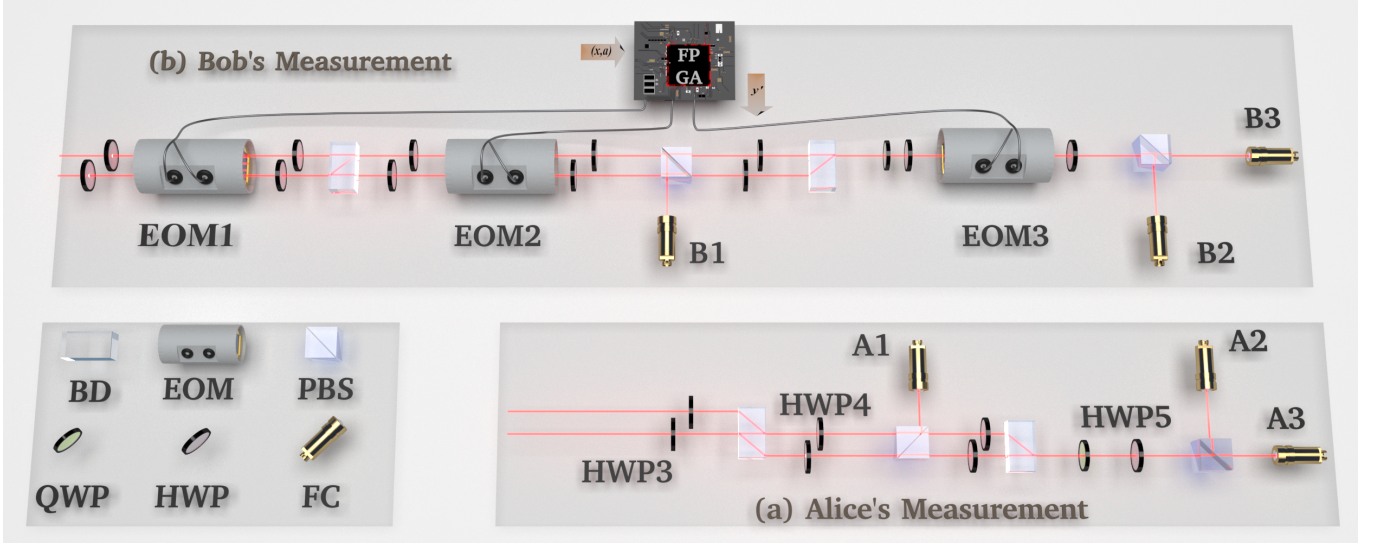


FIG. 4 **Experimental setup of local measurements.** Switching between the three measurement settings can be accomplished for both Alice and Bob measurements. (a) **Alice's Measurement**, the implemented bases are the computational basis, Fourier basis, and Gell-Mann basis, which are realized by tuning HWP3, HWP4, and HWP5 to the angles in table VI. (b) **Bob's Measurement**, real-time switching is realized by the fast configuration switching of extra EOM1-EOM3, with a repetition frequency of 10 MHz. Specifically, the two-level modes of EOM (offset or pulse) are switched by different Volts. The correspondence between the bases and configuration of EOMs is shown in the table VII.

ence light is attenuated to 10^6 Hz and finally detected by a single photon detector. The reference light in upper path is reflected by the mirror of a piezoelectric ceramic material (PZT) to change length of the optical path. After that, reference light in two paths is coupled into one end of 50m optical fiber and then emitted from the other end. Two beam displacers form a Mach-Zehnder interferometer. We use the PZT to adjust the position of the mirror according to the signal of the Mach-Zehnder interferometer to lock the phase of the optical fiber.

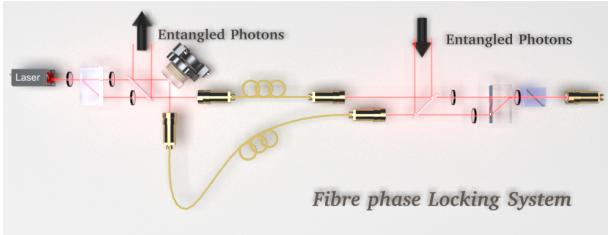


FIG. 5 **Fiber Locking System.** The reference light is divided into two beams by one beam displacer and recombined by another beam displacer, composing a Mach-Zehnder interferometer with two 50m optical fibers. A mirror of a piezoelectric ceramic (PZT) is used to change length of the optical path to lock the phase of two paths after 50m optical fiber according to the signal of reference light.

As shown in Fig. 6, we measure the visibility of entanglement photons between two paths to test the feedback system.

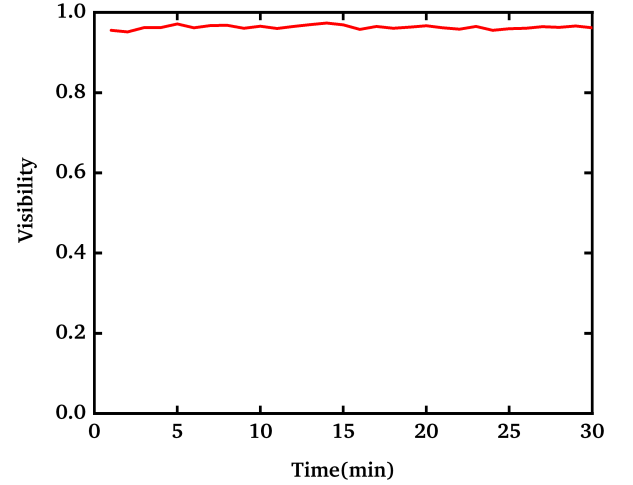


FIG. 6 **Interference visibility between two paths with active feed-back.** The average entanglement visibility of the two path interference in half an hour is $V = 0.963$.

Appendix F: Additional Analysis of Experimental Results

After completing the experiments, Tab. I shows that the advantage of extra classical information has been experimentally demonstrated, as the minimal false-negative probability for 1-LOCC is smaller than that of LO for the same false-positive probability of 0.7481. While the experimental p_2 values deviate from theoretical predictions, the discrepancy in the advantage is much smaller, indicating that errors

in p_2 have minimal impact on the observed advantage. Using the expectations of optimized protocols M_N^* as a metric, Tab.I shows that the false-negative errors for the estimated states ρ_{est}^{LO} and ρ_{est}^{1-LOCC} in both LO and 1-LOCC scenarios are closer to experimental false-negative errors than theoretical ones, while maintaining a low advantage discrepancy. Additionally, the fidelity between ρ_{est}^{LO} and ρ_{est}^{1-LOCC} is 94.34%, indicating that the shuffle strategy stabilizes the state for both LO and 1-LOCC.

The advantage of 1-LOCC is evident from the smaller p_2^{1-LOCC} compared to p_2^{LO} at the same p_1 . Experimental results confirm this with a 0.0611 gap in Eq. (5), despite some deviations from theoretical predictions. To support the experimental results, we conducted additional analysis using experimental data, shown in Fig.7. Here, ρ_{1-LOCC}^{est} (ρ_{LO}^{est}) is the experimentally estimated quantum state using existing raw data from the LOCC (LO) protocol, which may not tomographically complete (see Methods). We then performed optimistic estimates in Eq. (B2) and rerun SDR (??) for both inner approximation and outer approximation of the false negative error probability p_2 for the two quantum states under the LO measurement protocol.

As shown in Fig. 7, results for both quantum states are highly consistent under both approximations, suggesting the measurement strategy (Tables IV and V) effectively mitigates measurement-instability concerns. Most importantly, even under the optimistic estimate for LO, the experimental false-negative error probability p_2 for 1-LOCC remains lower, providing experimental evidence for the advantage of 1-LOCC. The remaining discrepancy from theoretical values is likely due to experimental imperfections.

TABLE I The p_1 , p_2^{LO} , p_2^{1-LOCC} , and G of theoretical, experimental and estimated states ρ^* , ρ_{exp} , ρ_{est}^{LO} , ρ_{est}^{1-LOCC} .

-	p_1	p_2^{1-LOCC}	p_2^{LO}	G
ρ^*	0.7481	0.0283	0.0944	0.0661
ρ_{exp}	0.7481	0.0779	0.1390	0.0611
ρ_{est}^{LO}	0.7481	0.0827	0.1402	0.0575
ρ_{est}^{1-LOCC}	0.7481	0.0812	0.1388	0.0576

TABLE II Adjustable angles of Half-Wave Plates (HWPs) and Liquid Crystals (LCs) used in the state preparation setup.

Stage 1	HWP 1	14.1008
	HWP 2	22.4197
	ϕ 1	-133.4403
Stage 2	ϕ 2	-116.7898
	ϕ 3	138.4193
	T_{21}^*	HWP 220.4253
		LC -24.2479
	T_{20}^*	HWP -22.3150
		LC -4.2391
	T_{10}^*	HWP -13.8507
		LC 100.6367

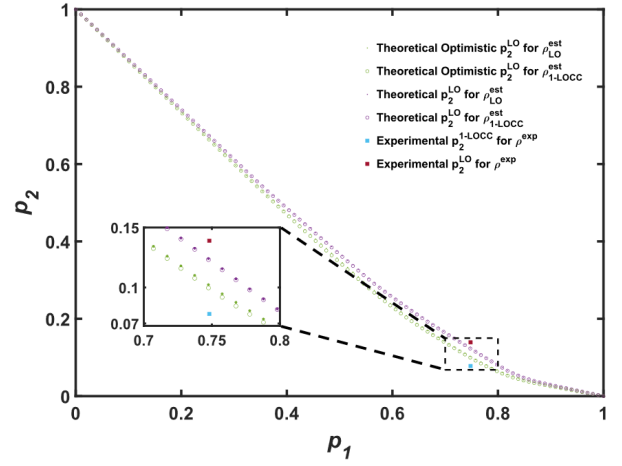


FIG. 7 The comparison of false-negative error probabilities p_2 s for false-positive error probabilities $p_1 \in [0, 1]$. The purple dots and circles represent approximations of p_2 in Eq. (??) for estimated states ρ_{est}^{LO} and ρ_{est}^{1-LOCC} under the LO scenario. The green markers show optimistic approximations in Eq. (B2) for the estimated states. Both approximations for the two estimated states almost overlap, demonstrating that the shuffle strategy stabilizes the state for both LO and 1-LOCC. The blue square indicates experimental p_2 s values under the 1-LOCC scenario (circle). It can be found that the experimental 1-LOCC p_2 (blue square) is below both optimistic estimates and pessimistic ones of LO. The red square represents the experimental p_2 value in the LO scenario.

TABLE III The small distributions $P(x)^* P(y|ax)^*$ for 1-LOCC protocols and $P(xy)^*$ for LO protocols.

x	$P(x)$	$a \ x \ P(1 ax) \ P(2 ax) \ P(3 ax)$			$x \ y \ P(xy)$	
		1	2	3	1	2
1	0.2020	0.0000	0.0378	0.9622	1	0.0000
2	0.4768	1.0000	0.0000	0.0000	1	0.1065
3	0.3212	0.0000	0.0000	1.0000	1	0.1290
2	0.4768	0.0000	1.0000	0.0000	2	0.3870
3	0.3212	1.0000	0.0000	0.0000	2	0.1672
3	0.3212	0.0000	0.0089	0.9911	2	0.0000
3	0.3212	0.0000	0.0139	0.9861	3	0.0000
3	0.3212	0.0000	1.0000	0.0000	3	0.0000
3	0.3212	0.2526	0.4960	0.2514	3	0.2103

TABLE IV The LO and 1-LOCC shuffled protocol $P_m(x)$

x	0	1	2
$P(x)$	0.2188	0.5155	0.2657

TABLE V The LO and 1-LOCC shuffled protocol $P_m(y'|ax)$

$a \ x$	$P(0 ax)$	$P(1 ax)$	$P(2 ax)$	$P(3 ax)$	$P(4 ax)$	$P(5 ax)$
1 1	0.0000	0.2435	0.2947	0.0000	0.0175	0.4443
1 2	0.3754	0.1622	0.0000	0.4624	0.0000	0.0000
1 3	0.0000	0.0000	0.3956	0.0000	0.0000	0.6044
2 1	0.0000	0.2435	0.2947	0.0000	0.4618	0.0000
2 2	0.3754	0.1622	0.0000	0.4624	0.0000	0.0000
2 3	0.0000	0.0000	0.3956	0.0000	0.0054	0.5990
3 1	0.0000	0.2435	0.2947	0.0000	0.0064	0.4553
3 2	0.3754	0.1622	0.0000	0.0000	0.4624	0.0000
3 3	0.0000	0.0000	0.3956	0.1527	0.2998	0.1519

TABLE VI Angles of HWPs to perform Alice's measurement.

	Computational	Fourier	Gell-Mann
HWP3	0°	-22.5°	-22.5°
HWP4	0°	17.6°	45°
HWP5	0°	22.5°	0°

TABLE VII Voltage of EOMs to perform Bob's measurement.

	Computational	Fourier	Gell-Mann
EOM1	offset	pulse	pulse
EOM2	offset	pulse	offset
EOM3	pulse	offset	pulse

TABLE VIII The optimal instructions of LO and 1-LOCC scenarios for ρ^*

x	y	a	b	$P_{LO}(xyN ab)$	$P_{1-LOCC}(xyN ab)$	x	y	a	b	$P_{LO}(xyN ab)$	$P_{1-LOCC}(xyN ab)$
1	1	1	1	0	0	2	2	2	2	0	0
1	1	1	2	0	0	2	2	2	3	0	0
1	1	1	3	0	0	2	2	3	1	0	0
1	1	2	1	0	0	2	2	3	2	0.1138	0
1	1	2	2	0	0	2	2	3	3	0.1672	0.4768
1	1	2	3	0	0	2	3	1	1	0	0
1	1	3	1	0	0	2	3	1	2	0	0
1	1	3	2	0	0	2	3	1	3	0	0
1	1	3	3	0	0	2	3	2	1	0	0
1	2	1	1	0	0	2	3	2	2	0	0
1	2	1	2	0.1065	0.0076	2	3	2	3	0	0
1	2	1	3	0.1065	0.0076	2	3	3	1	0	0
1	2	2	1	0.1065	0.202	2	3	3	2	0	0
1	2	2	2	0	0	2	3	3	3	0	0
1	2	2	3	0	0	3	1	1	1	0	0
1	2	3	1	0.0522	0.0028	3	1	1	2	0	0
1	2	3	2	0.0573	0.0028	3	1	1	3	0	0
1	2	3	3	0.0442	0	3	1	2	1	0	0
1	3	1	1	0	0	3	1	2	2	0	0
1	3	1	2	0.129	0.1453	3	1	2	3	0	0
1	3	1	3	0.129	0.1944	3	1	3	1	0	0.0811
1	3	2	1	0.0053	0	3	1	3	2	0	0.0811
1	3	2	2	0	0	3	1	3	3	0	0
1	3	2	3	0.129	0	3	2	1	1	0	0
1	3	3	1	0.129	0.1992	3	2	1	2	0	0
1	3	3	2	0.129	0.1992	3	2	1	3	0	0
1	3	3	3	0	0	3	2	2	1	0	0.0028
2	1	1	1	0.387	0.4768	3	2	2	2	0	0.0028
2	1	1	2	0	0	3	2	2	3	0	0
2	1	1	3	0.1836	0.046	3	2	3	1	0	0
2	1	2	1	0	0	3	2	3	2	0	0.1593
2	1	2	2	0.387	0.4768	3	2	3	3	0	0
2	1	2	3	0.1781	0.046	3	3	1	1	0	0
2	1	3	1	0.0639	0	3	3	1	2	0.2103	0.2145
2	1	3	2	0.0708	0	3	3	1	3	0.2103	0.3212
2	1	3	3	0.0455	0	3	3	2	1	0.2103	0.3183
2	2	1	1	0.0835	0	3	3	2	2	0.2103	0.3183
2	2	1	2	0	0	3	3	2	3	0	0
2	2	1	3	0	0	3	3	3	1	0.1576	0.0807
2	2	2	1	0.0841	0	3	3	3	2	0	0
-	-	-	-	-	-	3	3	3	3	0.2103	0.0807

TABLE IX The final decision distributions $P(N|abxy)^*$ for LO and 1-LOCC scenarios.

x	y	a	b	$P_{LO}(N abxy)$	$P_{1-LOCC}(N abxy)$	x	y	a	b	$P_{LO}(N abxy)$	$P_{1-LOCC}(N abxy)$
1	1	1	1	0.0000	0.0336	2	2	2	2	0.0000	0.5667
1	1	1	2	0.0000	0.0369	2	2	2	3	0.0000	0.0487
1	1	1	3	0.5000	0.5030	2	2	3	1	0.0000	0.0000
1	1	2	1	0.8333	0.9833	2	2	3	2	0.6806	0.0000
1	1	2	2	0.8333	0.9365	2	2	3	3	1.0000	1.0000
1	1	2	3	0.5000	0.0001	2	3	1	1	0.0000	0.0394
1	1	3	1	0.6667	0.3303	2	3	1	2	0.4000	0.5009
1	1	3	2	0.3333	0.2849	2	3	1	3	0.4000	0.5330
1	1	3	3	0.5000	0.7040	2	3	2	1	0.0000	0.0796
1	2	1	1	0.0000	0.0000	2	3	2	2	0.4000	0.5025
1	2	1	2	1.0000	1.0000	2	3	2	3	0.8000	0.7731
1	2	1	3	1.0000	1.0000	2	3	3	1	0.2000	0.5488
1	2	2	1	1.0000	1.0000	2	3	3	2	0.4000	0.0073
1	2	2	2	0.0000	0.0000	2	3	3	3	0.8000	0.6488
1	2	2	3	0.0000	0.0000	3	1	1	1	0.0000	0.1790
1	2	3	1	0.4900	1.0000	3	1	1	2	0.0000	0.0202
1	2	3	2	0.5383	1.0000	3	1	1	3	0.5000	0.5044
1	2	3	3	0.4153	0.0000	3	1	2	1	0.7500	0.3299
1	3	1	1	0.0000	0.0000	3	1	2	2	0.5000	0.2843
1	3	1	2	1.0000	0.7473	3	1	2	3	0.5000	0.7027
1	3	1	3	1.0000	1.0000	3	1	3	1	0.5000	1.0000
1	3	2	1	0.0410	0.9388	3	1	3	2	0.7500	1.0000
1	3	2	2	0.0000	0.0002	3	1	3	3	0.5000	0.0000
1	3	2	3	1.0000	0.9825	3	2	1	1	0.0000	0.0204
1	3	3	1	1.0000	1.0000	3	2	1	2	0.0000	0.0050
1	3	3	2	1.0000	1.0000	3	2	1	3	0.9913	0.9736
1	3	3	3	0.0000	0.0000	3	2	2	1	0.4957	1.0000
2	1	1	1	1.0000	1.0000	3	2	2	2	0.4870	1.0000
2	1	1	2	0.0000	0.0000	3	2	2	3	0.5130	0.0000
2	1	1	3	0.4744	0.0965	3	2	3	1	0.0087	0.0000
2	1	2	1	0.0000	0.0000	3	2	3	2	0.9913	1.0000
2	1	2	2	1.0000	1.0000	3	2	3	3	0.0087	0.0000
2	1	2	3	0.4600	0.0965	3	3	1	1	0.0000	0.0000
2	1	3	1	0.1652	0.5890	3	3	1	2	1.0000	0.6677
2	1	3	2	0.1829	0.6521	3	3	1	3	1.0000	1.0000
2	1	3	3	0.1176	0.0066	3	3	2	1	1.0000	1.0000
2	2	1	1	0.4993	0.7151	3	3	2	2	1.0000	1.0000
2	2	1	2	0.0000	0.4355	3	3	2	3	0.0000	0.0000
2	2	1	3	0.0000	0.0180	3	3	3	1	0.7493	1.0000
2	2	2	1	0.5027	0.8276	3	3	3	2	0.0000	0.0000
-	-	-	-	-	-	3	3	3	3	1.0000	1.0000